A|'

Mach Reflection from HE-Driven Blast Wave
P. Colella, R.E. Ferguson, H.M. Glaz, and A.L. Kuhl

Mach Reflection from an HE-Driven Blast Wave

P. Colella*

Lawrence Berkeley Laboratory, Berkeley, California

R.E. Ferguson† and H.M. Glaz†

Naval Surface Weapons Center, Silver Spring, Maryland

and

A.L. Kuhl‡

R&D Associates, Marina del Rey, California

Abstract

Flowfields associated with one-dimensional free-air explosions are well known both for the point-source case and for the case of a blast wave driven by the detonation of a high-explosive (HE) charge. Considered here is the two-dimensional case of the reflection of a spherical, HE-driven blast wave from an ideal plane surface. The evolution of the flowfield was calculated with a nondiffusive numerical algorithm for accurately solving the Euler equations. This algorithm is based on a second-order Godunov scheme and a monotonicity algorithm that is designed to give sharp shocks and contact surfaces while smooth regions of the flow remain smooth yet free of numerical diffusion. The incident HE-driven blast wave was accurately captured by a fine-zoned one-dimensional calculation that was continuously fed into the two-dimensional mesh. The latter incorporated a fine-zoned mesh that followed the reflection region and accurately resolved the complicated flow structure occurring on multiple length scales. Major findings in the regular reflection region were as follows. Portions of the main reflected shock were reflected within the channel formed by the wall and the reflected within the channel formed by the wall and the dense HE products, thus creating additional pressure pulses on the wall. Coherent vortex structures formed on the fireball as a result of the interaction of the reflected shock with this contact surface. The flow did

indeed make a transition to a double-Mach structure, but this transition was delayed 1.5 to 3.8 deg beyond the two-shock limit of regular reflection because the nascent Mach stem was less than one cell high in this region. The double-Mach structure with its two moving stagnation points was similar (but not identical) to an equivalent shock-on-wedge case. A key feature of this flow was a supersonic wall jet (velocity of 3.5 to 4.3 km/s) consisting of a free shear layer and a wall boundary layer. The wall jet was laminar in these calculations, but should actually be turbulent due to Reynolds number considerations. Nevertheless, calculated peak pressures were found to be in excellent agreement with experimental data at all ground ranges.

I. Introduction

Considered here is the two-dimensional axisymmetric reflection of a spherical (high-explosives-driven) blast wave from a plane surface. The temporal evolution of the flowfield was calculated with a second-order Eulerian Godunov scheme that accurately solves such inviscid compressible flow problems on a very fine computational mesh. The accuracy of the solution was confirmed by experimental pressure data for the same problem.

The details of flowfields associated with one-dimensional free-air explosions are well established. Consider, for example, the similarity solution of Taylor (1941) blast waves: the point explosion solution of Taylor (1941) and Sedov (1946), and all classes of blast waves bounded by strong shocks (Oppenheim et al. 1972a) and by strong Chapman-Jouguet detonations (Oppenheim et al. 1972b). Other examples are the non-self-similar solutions of the decay of a point-source explosion: the original finite-difference calculation (Von Neumann and Goldstine 1955), the method of integral relations solution (Korobeinikov and Chushkin 1966), the method of characteristics solution (Okhotsimskii et al. 1957), and the Lagrangian finite-difference calculations (Brode 1955). Also well established are non-self-similar solutions of the decay of spherical blast waves driven by a solid, high-explosives (HE) charge (Brode 1959).

However, when one considers the reflection of such spherical blast waves from a plane surface, a detailed description of the flowfields is not generally available. Such flows are inherently two dimensional. They are driven by decaying blast waves, and hence they are intrinsically non-self-similar. They depend parametrically on the

scaled height of burst (HOB) of the explosion, the blast source, and the equation of state (EOS) of the medium (e.g., γ varies for real air). Hence, such flowfields are not amenable to general solution; each represents a particular case.

Much of our knowledge of such reflections comes from considering the flowfield in the near vicinity of the reflection point. By neglecting the rarefaction wave behind the incident shock, one can equate the flow to that produced by a plane, square wave shock reflecting from a plane surface. This is, of course, a good approximation when the flow behind the reflected shock is supersonic (relative to the reflection point). Many tools then become available. For example, one can use the shock polar technique (Courant and Friedrichs 1948) with an appropriate equation of state to predict peak pressures in the regular reflection regime; whereas in the Mach reflection regime, one must resort to experimental data of shock reflections from wedges (e.g., Bertrand 1972). One can use experimental shock-on-wedge results and their associated empirical theories to predict the transition to Mach reflection and the approximate shock structure.[*] Indeed, such analysis predicts that for strong shocks, transition will proceed from regular to double-Mach reflection. One can even view the height-of-burst problem as a continuous sequence of shock-on-wedge configurations for which the wedge angle varies from 90 deg at ground zero to 0 deg at an infinite ground range. Nevertheless, such techniques have a limited utility. They are always approximations to a truly non-self-similar problem, and they do not describe the entire flowfield. To overcome such limitations, one must resort to height-of-burst experiments and two-dimensional numerical simulations.

Height-of-burst experiments utilizing HE blast wave sources have been conducted (Baker 1973). Typically, flowfield measurements are limited to near-surface static and total pressure histories at a small number of ground ranges, and high-speed photography. Often there is much scatter in the data due to nonrepeatability of the HE charges; this scatter limits the scientific usefulness of the data. Some of the most repeatable data come from tests performed with 8-lb spheres of PBX-9404 (Carpenter 1974). Nevertheless, such measurements are not sufficient

---

[*]See, for example, Ben-Dor and Glass (1978, 1979), Ando and Glass (1981), Shirouzu and Glass (1982), Lee and Glass (1984), Deschambault and Glass (1983), Bazhenova et al. (1984), Hu and Glass (1986), Hornung (1985), and Hornung and Taylor (1982).

to allow one to reconstruct the entire flowfield. For that, a numerical simulation of the flow is required.

Today, one can simulate the reflection of a spherical blast wave from a plane surface with numerical codes that solve the inviscid two-dimensional Euler equations of gasdynamics: for example, a simulation of the Tunguska meteorite explosion at an HOB = 305 m/kt[3] (Shurshalov 1978) and the calculation of a point-source case detonated at an HOB = 31.7 m/kt[3] (Fry et al. 1981). How accurate are such calculations? One of the difficulties in numerical simulation of such flows is the disparity of length scales in the problem; for example, the height-of-burst scale vs the Mach stem height (typically less than 1/10 the height-of-burst scale) vs the boundary layer scale (which is much smaller than the Mach stem height). One must take special care to design the computational mesh to take such disparate length scales into account. With the memory size and speed of class VI computers such as the CRAY 1, such large-scale computations are now possible (although expensive). Of course, one needs a minimal-diffusion numerical algorithm to maximize the information per grid point. A noteworthy example is the second-order Eulerian Godunov scheme of Colella and Glaz (1984, 1985). This code has been used to simulate shock-on-wedge experiments in the regular reflection regime and in the simple, complex, and double-Mach reflection regimes. Excellent agreement with data was obtained for those cases for which viscous and nonequilibrium effects were negligible in the experiments (Glaz et al. 1985a, 1985b, 1986). In some of the double-Mach reflection cases for which such effects were not small, qualitative agreement was still found for flowfield features such as contact surface/second Mach stem interaction and subsequent vortex rollup. Nevertheless, the question remains: How accurately can one numerically simulate the truly nonsteady height-of-burst case?

The objective of this work was then to perform a highly resolved numerical simulation of the two-dimensional reflection of an HE-driven blast wave with the abovementioned Godunov scheme and to check the accuracy of the solution by comparing it with precision experimental data. An 8-1b PBX-9404 charge experiment detonated at HOB = 51.66 cm (Carpenter 1974) was selected for that purpose. A zoning convergence study (with a fine grid mesh spacing of 1.2, 0.6, and, finally, 0.3 mm) was performed to demonstrate that the results were independent of cell size.

The computational technique including the second-order Godunov scheme, the equations of state, the initial conditions, and the grid dynamics are described in Sec. II.

The numerical results, such as the incident one-dimensional blast wave, the regular reflection regime, transition, the double-Mach reflection regime, comparisons of surface data, and comparisons with an equivalent shock-on-wedge case, are presented in Sec. III. Conclusions and recommended improvements are offered in Sec. IV.

II. Computational Method

The equations of compressible hydrodynamics in one space variable, written in conservation form, are

$$\frac{\partial}{\partial t} \underline{U} + \frac{\partial}{\partial V} A\underline{F} + \frac{\partial}{\partial r} \underline{H} = 0 \qquad (1a)$$

where

$$\underline{U} = \begin{Bmatrix} \rho \\ \rho u \\ \rho v \\ \rho E \\ \rho X \end{Bmatrix}, \quad \underline{F}(U) = \begin{Bmatrix} \rho_2 \\ \rho u \\ \rho uv \\ \rho uE + up \\ \rho uX \end{Bmatrix} \underline{H}(U) = \begin{Bmatrix} 0 \\ p \\ 0 \\ 0 \\ 0 \end{Bmatrix} \qquad (1b)$$

Here, ρ is the density; $E = (1/2)(u^2 + v^2) + e$ is the total energy per unit mass, where e is the internal energy per unit mass, u is the component of velocity in the r-direction, and v is the transverse component of velocity; p is the pressure; X represents an arbitrary advected scalar quantity; and $V \equiv V(r) = r^{\alpha+1}/(\alpha + 1)$ is a volume coordinate, $A \equiv A(r) = dV/dr = r^{\alpha}$. The values $\alpha = 0,1,2$ correspond to Cartesian, cylindrical, and spherical symmetry, respectively. This particular representation of the equations follows Colella and Woodward (1984) and corresponds closely to the finite-difference equations that follow.

The pressure is given by an equation of state:

$$p \equiv p(\rho, e) \qquad (2)$$

for single-fluid hydrodynamics. For the calculations presented here, it is necessary to use a two-fluid model, where the two fluids are the detonation product gases and air. Each of these materials has associated with it an equation of state of the form of Eq. (2). We let X denote the volume fraction of high explosives (HE), so that in a mixed cell, $0 < X < 1$. Then our two-fluid treatment is defined by the last equation in Eq. (1) and by setting

$$p = Xp_{HE} + (1-X)p_{air} \qquad (3)$$

wherever a pressure is needed by the numerical method. This relatively crude treatment (in particular, our reliance on the mixture density and internal energy precludes referring to the model as a true two-fluid model) turns out to be sufficient for the present problem. This is largely due to the fact that the dynamics of the material interface are not of major interest and they do not directly interact with the Mach stem region flowfield, which is the focal point of this study. Our treatment here will be superseded by a true multimaterial algorithm based on the simple line interface calculation (SLIC) algorithm of Noh and Woodward (1976) and the Eulerian second-order Godunov scheme for single-fluid hydrodynamics (Colella et al. 1986).

The numerical method used in this study is the version of the second-order Eulerian Godunov scheme described in Colella and Glaz (1985). This version was especially designed to handle general equations of state of the type encountered here. The modifications necessary for non-Cartesian symmetries (i.e., $\alpha = 1,2$) are described in Colella and Woodward (1984). Operator splitting is used to solve multidimensional problems; in the axisymmetric calculation of Sec. III, this means that Eqs. (1) with $\alpha = 1$ are solved in the radial direction with u set to the radial component of velocity; and then Eqs. (1) with $\alpha = 0$ are solved in the axial direction with u set to the axial component of velocity. A brief overview of the method for solving Eqs. (1) is presented below.

Let $U^n = \{U^n_j\}$ represent the cell-averaged solution at time level $t = t^n$, i.e.,

$$U^n_j = (\Delta V_j)^{-1} \int_{V^n_{j-1/2}}^{V^n_{j+1/2}} U(r,t^n)dV \qquad (4)$$

The computational objective is to define U^{n+1} in terms of U^n. The conservative, second-order-in-time, finite-difference representation of Eqs. (1) is

$$\Delta V^{n+1}_j U^{n+1}_j = \Delta V^n_j U^n_j - \Delta t^n \left[A^{n+1/2}_{j+1/2} F^{n+1/2}_{j+1/2} - A^{n+1/2}_{j-1/2} F^{n+1/2}_{j-1/2} \right.$$
$$\left. + \left(H^{n+1/2}_{j+1/2} - H^{n+1/2}_{j-1/2} \right) \frac{2.0}{\Delta r^n_j + \Delta r^{n+1}_j} \right] \qquad (5)$$

where

$$\Delta V_j = V_{j+1/2} - V_{j-1/2}, \qquad V_{j+1/2} \equiv V(r_{j+1/2})$$

$$A^{n+1/2}_{j+1/2} = (\Delta t^n)^{-1} \int_0^1 A \left[r^n_{j+1/2} + \beta (r^{n+1}_{j+1/2} - r^n_{j+1/2}) \right] d\beta$$

Here, typical $F^{n+1/2}_{j+1/2} = F(U^{n+1/2}_{j+1/2})$, and $U^{n+1/2}_{j+1/2}$ represents the average of U along the (j,j+1) interface, i.e.,

$$U^{n+1/2}_{j+1/2} = (\Delta t^n)^{-1} \int_{t^n}^{t^{n+1}} U \left[r^n_{j+1/2} + s^{n+1/2}_{j+1/2} (t - t^n), t \right] dt$$

where

$$s^{n+1/2}_{j+1/2} = \left(r^{n+1/2}_{j+1/2} - r^n_{j+1/2} \right) \Big/ \Delta t^n$$

Evidently, a computational scheme in the form Eq. (5) is defined by specifying $U^{n+1/2}_{j+1/2}$ as a function of U^n.

The first-order Godunov scheme is defined by setting $U^{n+1/2}_{j+1/2}$ to the solution of the Riemann problem (U^n_j, U^n_{j+1}) evaluated along the line $r/t = s^{n+1/2}_{j+1/2}$. The high-order scheme is conceptually similar in that a Riemann problem $(U^n_{j+1/2,L}, U^n_{j+1/2,R})$ is constructed and solved in the same way. However, the left and right states are now functions of $(U^n_{j-2},...,U^n_{j+2})$ and $(U_{j-1},...,U_{j+3})$, respectively. These additional data are used to create monotonized piecewise-linear profiles in each computational zone, from which a version of the method of characteristics is based to get new values centered on the interface. The overall construction, including the solution of the Riemann problem, is equivalent to the method of characteristics (up to second order) for smooth flow in determining the interface fluxes. Further details, such as monotonicity constraints and additional constructions necessary near strong discontinuities, may be found in the references mentioned.

An important aspect of our numerical method is that we do not require equation-of-state evaluations at each step in the Riemann problem iterative solution; it is only necessary for the approximate method that the equation of state be evaluated for each U^n_j. The information required by the algorithm is the dimensionless quantities $\gamma \equiv \gamma(\rho,e)$, $\Gamma \equiv \Gamma(\rho,e)$ such that

$$p = (\gamma-1)\rho e \qquad (6)$$

and

$$c^2 = \Gamma p / \rho \qquad (7)$$

where c is the speed of sound. Note that $\gamma \neq \Gamma$ for a non-polytropic equation of state.

The equations of state used in the calculations of Sec. III are the equilibrium air EOS of Gilmore (1955) and Hansen (1959), and the Jones-Wilkins-Lee (JWL) EOS for PBX-9404 detonation product gases (Dobratz 1974). The caloric JWL equation of state takes the form

$$p = A(1-\omega\rho_0/R_1\rho)e^{-R_1\rho_0/\rho} + B(1-\omega\rho_0/R_2\rho)e^{-R_2\rho_0/\rho} + \omega\rho e \qquad (8)$$

whereas the isentrope is given by

$$p_s = Ae^{-R_1\rho_0/\rho} + Be^{-R_2\rho_0/\rho} + C(\rho_0/\rho)^{-(\omega+1)} \qquad (9)$$

where ρ_0 is the initial charge density and the JWL parameters for PBX-9404 are $A = 8.545$ Mbars; $B = 0.2049$ Mbars; $C = 0.00754$ Mbars; $R_1 = 4.60$; $R_2 = 1.35$; $\omega = 0.25$. The behavior of γ for the JWL EOS may be found by fitting Eq. (6) to Eq. (8), and $\Gamma(\rho,e)$ can be calculated from the isentrope using Eq. (9); in this case, c^2 is obtained in closed form (Glaz 1979) and Eq. (7) may be used to calculate Γ.

The calculation was run in two stages: first as a one-dimensional free air burst until ground strike, and then as a two-dimensional reflection problem. The one-dimensional calculation was initialized when the detonation wave reached the charge radius R_c. The flowfield inside the charge at that time was assumed to be that of an ideal Chapman-Jouguet (CJ) detonation (Taylor 1950; Kuhl and Seizew 1978) with no afterburning. Using the JWL parameters for a PBX-9404 charge with an initial density of $\rho_0 = 1.84$ g/cm^3, the CJ state is $p_{CJ} = 370$ kbars; $\rho_{CJ} = 2.485$ g/cm^3; $e_{CJ} = 8.142\times10^{10}$ erg/g; $W_{CJ} = 8.8$ km/s; $u_{CJ} = 2.28$ km/s; $q_{CJ} = 5.543\times10^{10}$ erg/g; $\Gamma = 2.85$; $X = 1$. For an 8-lb sphere the charge radius was $R_c = 7.76$ cm. The ambient atmosphere was initialized as $p_a = 1.00$ bar; $\rho_a = 1.1687\times10^{-3}$ g/cm^3; $e_a = 2.1390\times10^9$ erg/g; $u = 0$; $X = 0$. A fine-zoned grid ($\Delta r = 0.3$ mm) was dynamically moved with the shock to accurately capture the complex flow in that region. Coarse zones ($\Delta r = 3$ mm) were used near $r = 0$ and for large r; and a transition region connected these cells with the fine grid. After initialization, the evolution of the one-dimensional blast wave was calculated by solving Eqs. (1) with $\alpha = 2$ until the shock radius was equal to the height of burst (51.66 cm; $t =$

97.44 μs). This solution was then conservatively interpolated onto a two-dimensional mesh.

The two-dimensional mesh covered a region $0 < r < 100$ cm and $0 < z < 20$ cm (617 r cells by 214 z cells). Note that the top of the grid was below the height of burst to pack as many cells near the wall as possible. During the computation, the reflected shock never reached the upper boundary; consequently, it could be treated with a time-dependent Dirichlet boundary condition. The Dirichlet data were provided by continuing to update the one-dimensional solution for each step of the two-dimensional calculation and feeding this solution into the top boundary. The bottom boundary was treated as an ideal (slip flow) reflecting plane. The left and right boundaries were treated as a symmetry line and an outflow boundary, respectively. A uniform fine-grid region (267 r cells by 140 z cells) with $\Delta r = \Delta z = 0.3$ mm was dynamically moved to follow the rightmost shock (the incident wave at early times and the Mach stem at late times). Again, transition and coarse cells ($\Delta r = \Delta z = 3$ mm) were used around the fine-grid region. The two-dimensional calculation was continued until the Mach reflection point reached 80 cm (270 μs). This required 3200 computational steps and about 9 h CP time on the CRAY 1.

III. Results

A. Incident HE-Driven Blast Wave

In 1959, Brode performed a pioneering calculation of a spherically symmetric blast wave driven by the detonation of a spherical TNT charge (initial charge density of 1.5 g/cm^3, detonation pressure of 157 kbars). The one-dimensional Lagrangian finite-difference scheme used the artificial viscosity technique (Von Neumann and Richtmeyer 1950) to capture shock fronts, and variable gamma equations of state to describe the air and detonation products gases. He found that an extremely strong rarefaction wave was created when the detonation wave reached the radius of the charge. This rarefaction accelerated the detonation products to a velocity of about 5.5 km/s. The interface or contact surface, CS, between the air and the detonation products acted like a spherical piston—thus creating an air shock (maximum peak pressure of about 400 bars). The resulting blast wave behaved like a decaying piston-driven blast wave (Sedov 1959) for shock pressures greater than about 7 bars, and approached the point-source similarity solution thereafter. The aforementioned rarefaction wave

caused the detonation products to overexpand to a velocity larger than that induced by the air shock. This incompatibility was resolved by an inward-facing shock, which eventually imploded and created a series of secondary pulses at late times.

Our calculation was performed for a spherical PBX-9404 charge (initial charge density of 1.84 g/cm^3 detonation pressure of 370 kbars). The resulting blast wave was qualitatively similar to Brode's results; hence, the results will not be reported here in detail. Quantitative differences were as follows. Peak velocities reached about 17 km/s, whereas the maximum peak air-shock pressure reached about 1 kbar, owing to the larger detonation pressure of the PBX charge. The blast wave approached the point-source solution at a shock overpressure of about
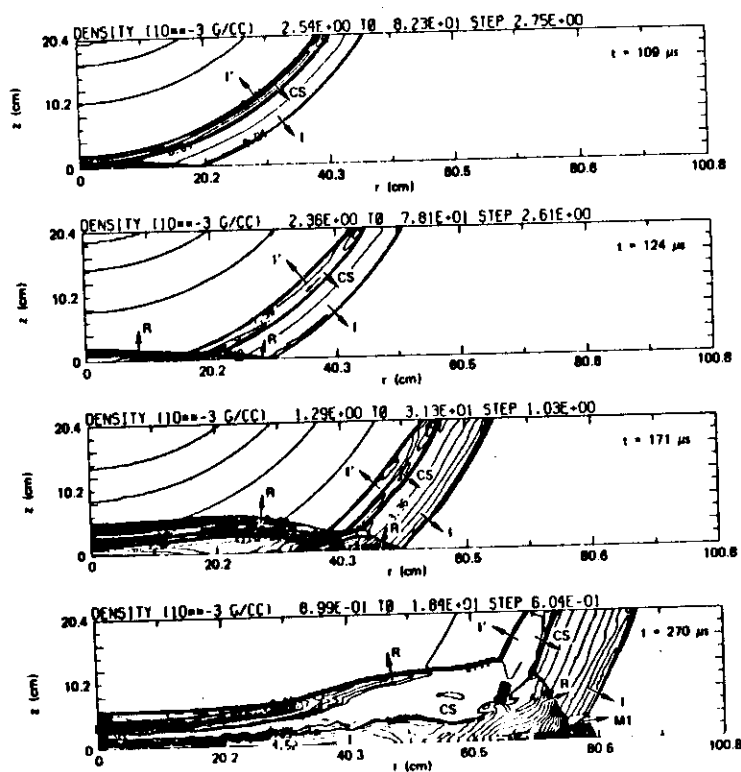

Fig. 1a   Transition from regular to double-Mach reflection for a spherical, HE-driven blast wave reflecting from an ideal plane surface. Density contours (10^{-3} g/cm^3).
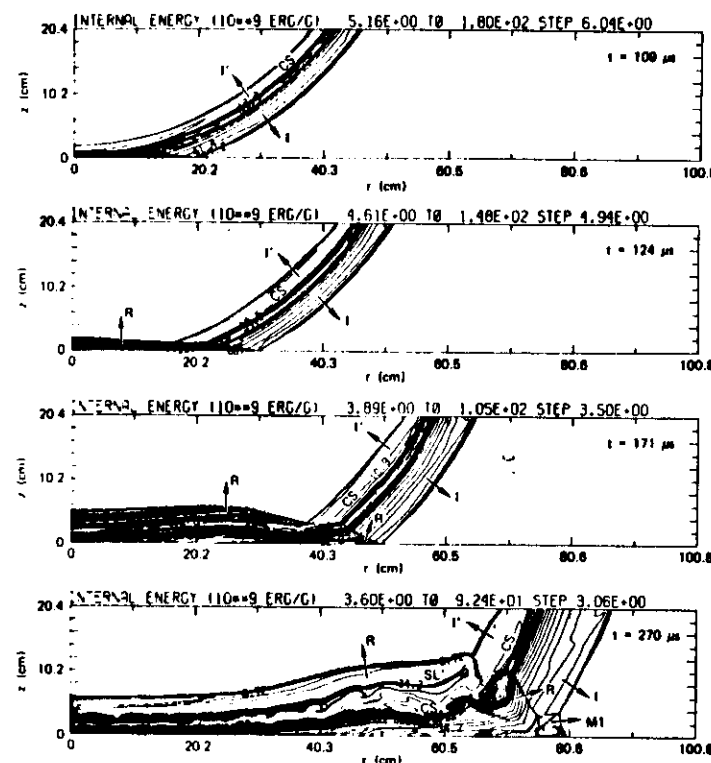
Fig. 1b   Transition from regular to double-Mach reflection for a spherical, HE-driven blast wave reflecting from an ideal plane surface. Internal energy contours (10^9 erg/g).

13 bars vs 7 bars for TNT. The air shock arrived at ground zero (i.e., at a shock radius corresponding to the HOB = 51.66 cm, or 6.78 charge radii) with an incident over-pressure of 98.86 bars; hence, the flowfield corresponded to a piston-driven wave throughout the entire regime of the two-dimensional calculation. This led to shock interactions that are unique to the HE case.

B. Overall View of the Two-Dimensional Reflection

An overall view of the two-dimensional reflection of the spherical HE-driven blast wave from an ideal plane surface is depicted in Fig. 1 in terms of isodensity, iso-internal energy, and isopressure contours at different times. Thirty equally spaced contour values were used, with the minimum and maximum value and step size identi-
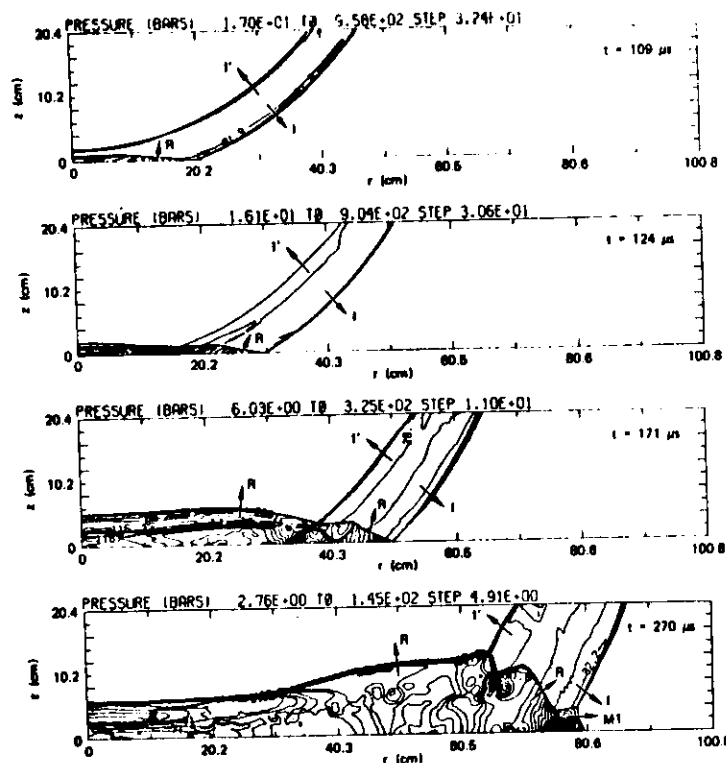
Fig. lc Transition from regular to double-Mach reflection for a spherical, HE-driven blast wave reflecting from an ideal plane surface. Pressure contours (bars).

fied on the plot. This technique gives a concise display of the major features of the two-dimensional flowfield: Discontinuities appear as heavy dark lines (where many contours group together), rarefaction waves appear as a fan of contour lines, while plateau regions are contour-free. Contact surfaces may be identified as discontinuities in density and internal energy, without any jump in pressure or velocity; slip lines may be distinguished as contact surfaces with a discontinuous change in velocity; shocks are denoted by discontinuities with sharp jumps in pressure.

In Fig. 1, the incident shock (I), the contact surface (CS) separating the detonation products and air, and the inward-facing shock (I') of the incident blast wave are clearly visible. Reflection of the incident shock I from the plane surface creates the main reflected shock R, which effectively stops the contact surface CS. At small

ground ranges, the reflected shock propagates upward very slowly because of the large, downward-directed dynamic pressure of the detonation products gases of the incident wave. This is markedly different from the case of the reflection of a point explosion blast wave in which the reflected shock propagates very rapidly through the low-density, high-sound-speed region near the blast center (Fry et al. 1981).

Interactions of the reflected shock R with the contact surface CS and the shock I' create additional shocks near the ground and generate vortex structures on CS and SL',
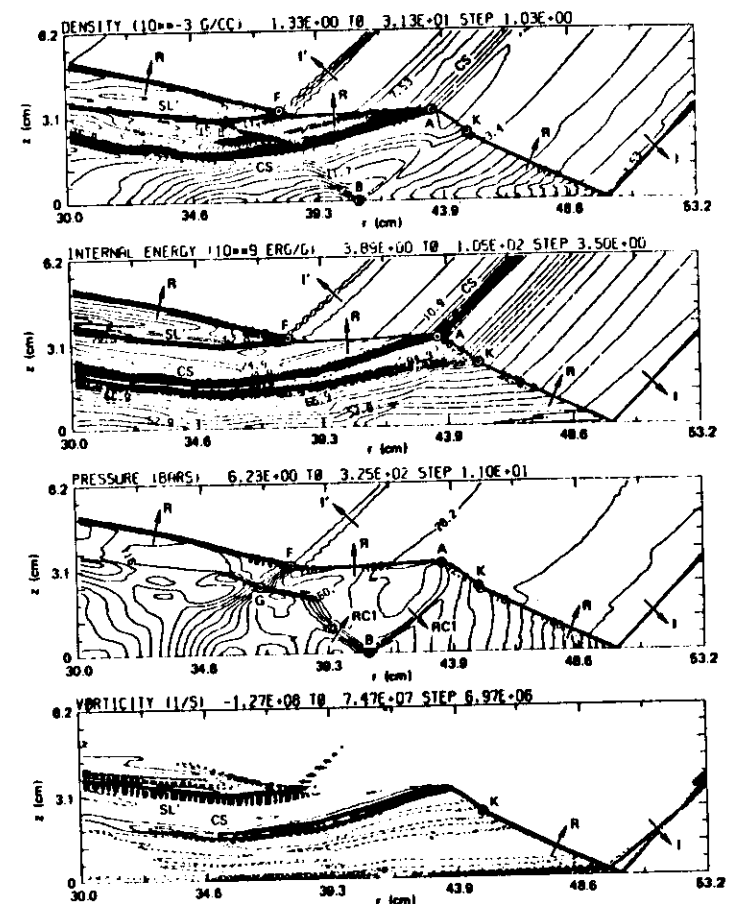

Fig. 2a Interaction of the reflected wave R with the contact surface CS and shock I' in the regular reflection regime (t = 171 μs; reflection point at 50 cm).
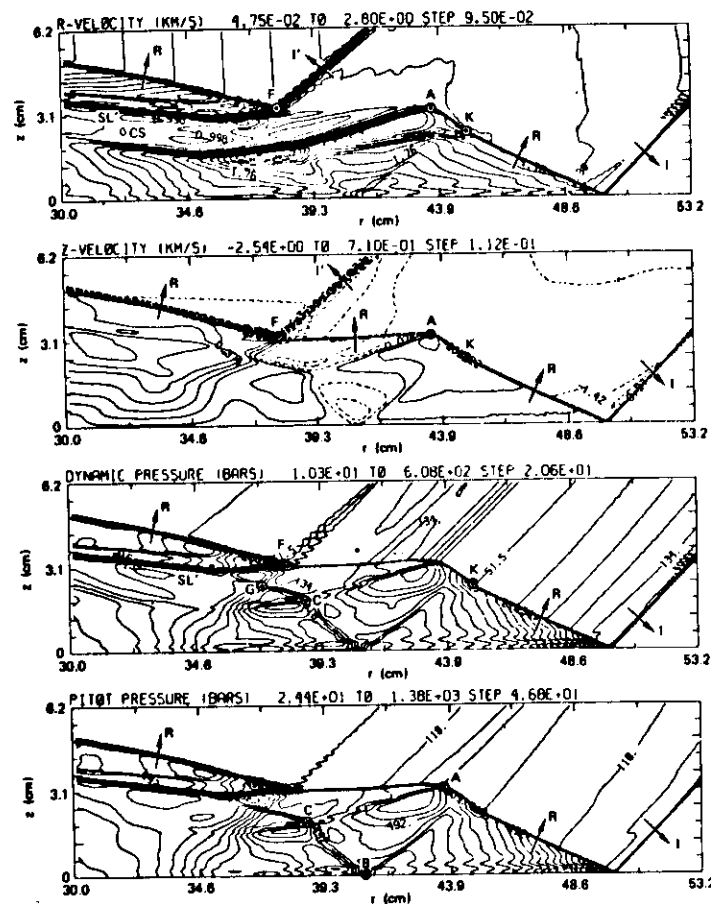
Fig. 2b Interaction of the reflected wave R with the contact surface CS and shock I' in the regular reflection regime (t = 171 µs; reflection point at 50 cm).

as shown in Figs. 1a and 1b. The reflected shock also deflects the contact surface away from the Mach stem region so that in this calculation, the detonation products are not entrained in the Mach stem flow.

C. The Regular Reflection Region

A detailed view of the flowfield near the end of the regular reflection region (t = 171 µs, reflection point at 50 cm) is shown in Figs. 2a and 2b. The weaker discon-

Fig. 2c. Interaction of the reflected wave R with the contact surface CS and shock I' in the regular reflection regime. Schematic showing wave interactions: (a) t = 124 µs, r = 30 cm; (b) t = 145 µs, r = 40 cm; (c) t = 171 µs, r = 50 cm.

tinuities are somewhat difficult to pick out when they are located in the coarse-zoned region; hence they have been depicted schematically in Fig. 2c.
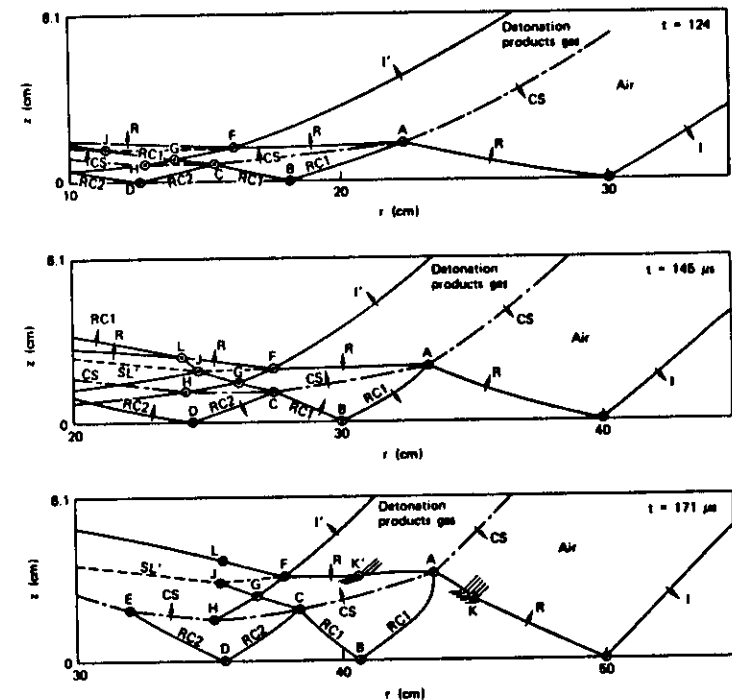
The reflected shock R interacts with the incident-wave contact surface CS at point A, creating a reflected shock RC1 and deflecting CS. Shock RC1 reflects off the wall at point B as a regular reflection, thus creating a second peak pressure on the wall. The reflected portion of RC1 reflects off contact surface CS at point C, creating reflected shock RC2, and further deflects contact surface CS. Shock RC2 reflects off the wall at point D as a regular reflection, thus creating a third peak pressure on the wall. The reflected portion of shock RC2 reflects off contact surface CS at point E, creating a third reflected shock RC3.

The transmitted portion of shock R emanating from point A interacts with the incident shock I' (oblique shock interaction) at point F, creating a slip line SL'.

The transmitted portion of shock I' emanating from point F interacts obliquely with the transmitted portion of shock RC1 emanating from C at point G; transmitted shocks from RC1 emanating interact with the contact surface CS at this reflection interact with the contact surface CS at point H, and with slip line SL' at J. At earlier times, a point reflected shock from point J interacted with the main transmitted shock at point L. Density/internal energy gradients in the incident wave cause kinks in the main reflected wave at points K and K'.

In summary, the following features were found in the regular reflection region. The main reflected wave R reflects within the channel formed by the wall and the dense detonation products (CS), causing additional pressure pulses on the wall. Shock interactions with contact surfaces at points A and F inviscidly generate positive and negative vorticity, respectively, which rolls up into vortex structures shown in Figs. 1a and 1b. Finally, the main contact surface CS is idealized in this calculation as a discontinuity. We know experimentally, however, that this surface is irregular and diffused--perturbations on this surface grow owing to a Rayleigh-Taylor mechanism and these lead to local turbulent mixing during the evolution of the incident blast wave (Anisimov et al. 1983). The strength of reflected shocks RC1 and RC2 will depend on the mixing across the contact surface CS. These inviscid calculations, which do not take into account such turbulent mixing, no doubt overestimate the strength of shocks RC1 and RC2.

Table 1 Comparison of regular double-Mach transitions

Source	Wedge angle, θ (deg)	Incident shock angle, α (deg)	Transition ground range (cm)
Limit of regular reflection			
Kuhl, 1982 (Gilmore's Air EOS [Gilmore 1955])	47	43	48.2
Glass, 1982 (Hansen's Air EOS [Hansen 1959])	46	44	49.9
HOB calculation			
PRR	45.5	44.5	52.5
DMR	43.2	46.8	55

D. The Transition Regime

A detailed view of the shock structure in the transition region is given in Fig. 3. In this calculation, transition from regular reflection (RR) to double-Mach reflection (DMR) occurred at a ground range of greater than 52.5 cm and less than 55 cm, with corresponding incident shock angles of 44.5 and 46.8 deg, respectively. Comparison with the limit of existence regular reflection (i.e., the so-called deflection criterion) for real air in Table 1 indicates that the calculated regular reflection region persisted in this height-of-burst calculation for 1.5 to 3.8 deg beyond the theoretical limit. Note that a similar persistence of regular reflection (PRR) has been
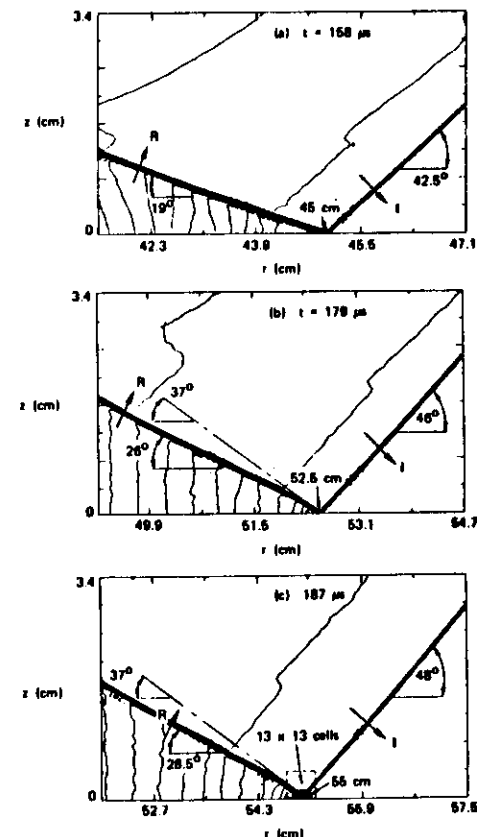

Fig. 3) Pressure contours showing transition from regular to double-Mach reflection: (a) t = 158 μs, r = 45 cm (RR); (b) t = 179 μs, r = 52.5 cm (PRR); (c) t = 187 μs, r = 55 cm (DMR).

observed for shock reflections from wedges, both experimentally (Bleackney and Taub 1949; Henderson and Lozzi 1975) and numerically, with the same hydrocode used here (Glaz et al. 1985a, 1985b, 1986).

One can identify three potential reasons for persistence of regular reflection: 1) real viscosity, 2) numerical viscosity, and 3) inadequate zoning. Real viscosity must be rejected for this case because it was not included in the calculation. The second-order Godunov scheme used here leaves essentially no numerical viscosity in the smooth regions of the flow. However, all shock-capturing schemes introduce numerical dissipation at shock fronts to allow a smooth transition between preshock and postshock states. When such algorithms are used to calculate shock waves near a wall, a "numerical wall boundary layer" is formed (Noh 1976). The primary effect of this is to create an artificial "wall heating"—typically a few percent. This effect can be seen in the density and radial velocity contours of Fig. 2, which exhibit a kink at about the 3-mm height (about ten cells).

A concerted effort was made to minimize computational cell-size effects. The 617 by 214 grid used essentially all of the one-megaword fast core space available on a CRAY 1 computer. The fine-zoned grid (267 by 140 cells) that slid with the reflection region used cells of 0.3 by 0.3 mm. This resulted in 83 radial cells between the reflection point at 52.5 cm and the 55-cm point, and one would think that would constitute adequate zoning. However, the Mach stem grows from a point (in the inviscid theory) and is never captured computationally until the shock structure grows large enough to be resolved on the mesh. Note that at the 55-cm location, the Mach stem was only about four cells high. If a Mach stem existed at the 52.5-cm ground range, it would be less than one cell high; hence, it would not have been resolved. A more detailed inviscid calculation of transition using a local adaptive grid refinement (e.g., Berger and Colella 1986) is required to conclusively resolve this zoning question. We speculate that such inviscid calculations will indeed confirm that double-Mach reflection will exist immediately after passing the RR limit. Therefore, we believe that the persistence of regular reflection in these calculations is caused by inadequate zoning and the numerical wall boundary layer, while the persistence behavior observed in experiments is due to a viscous wall boundary effect. To conclusively prove the latter, a viscous calculation of the oblique shock structure at the wall is required.

Peculiar gasdynamic effects were observed in this calculation in the PRR region. It is well known that as the incident shock angle increases in the regular reflection region, one encounters the sonic criterion (where sound waves can reach all the way to the reflection point) about 1 deg before one reaches the RR limit (Henderson and Lozzi 1975). In such a case, the reflected shock is no longer straight but continuously curved near the reflection point. The present calculations also exhibit such effects. Figure 3 shows that the reflected shock is straight at a ground range of 45 cm (RR) but curved near the reflection point at 52.5 cm. As shown in Table 2, the angle of the main portion of the reflected shock increases smoothly through transition; however, at the wall it jumps from about 24 deg at the 50-cm range to about 37 deg at the 52.5-cm range.

The pressure and velocity profiles on the wall also changed dramatically in the PRR region. When the reflection point was at 45 cm, the pressure and velocity gradients were well behaved. However, in the PRR region (e.g., with the reflection point at 52.5 cm), the pressure and velocity gradients on the wall become very large as one approaches the reflection point from the left.

In summary, the limit of regular reflection for this case is 43 to 44 deg (depending on the particular equation of state used for air) with a corresponding ground range to transition of 48.2 to 49.9 cm. In this calculation, regular reflection seemed to persist to a ground range of about 52.5 cm ($\alpha = 44.5$ deg), but the reflected shock

Table 2 Shock angles near transition

Ground range (cm)	Incident shock angle, α (deg)	Reflected shock angle		Regime
		Off wall, β(deg)	Near wall, β_o(deg)	
45	42.5	19	19	RR
50	44	24	24	PRR
52.5	46.5	26	~37	PRR
55	48	28.5	~37	DMR
57.5	49	33	~37	DMR
60	51	34	~37	DMR

angle near the surface at this range was consistent with
that of double-Mach reflection ($\beta \approx 37$ deg). Hence, we
believe that it was indeed a nascent double-Mach structure
that was not computationally resolved on the mesh. As we
shall see in the next section, both local adaptive mesh
refinement and turbulence modeling are required to prop-
erly model certain details of the flow in the double Mach
region and, by implication, to accurately predict transi-
tion.

E. The Double-Mach Region

A detailed view of the complex flowfield in the
double-Mach region is presented in Fig. 4 ($t = 270$ μs,
Mach stem at 80 cm). The domain of these figures repre-
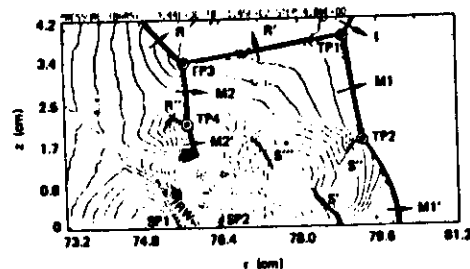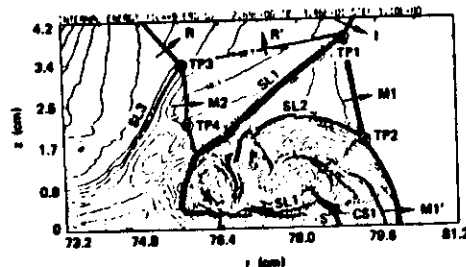sents the fine-zoned region of the calculation (267 r by
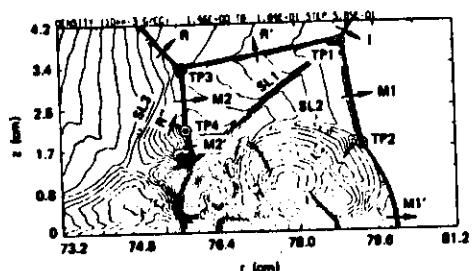
140 z cells with a cell size of 0.3 mm). The incident
shock (I), the reflected shock (R'), and the main Mach
stem (M1) meet at the main triple point (TP1), generating
a slip line (SL1) that has positive vorticity. Air flows
along SL1 and impacts on the wall, thus creating a large
local pressure. This point actually corresponds to a
moving stagnation point (SP1), which is particularly evi-
dent in the relative vector velocity plot of Fig. 4c (the
coordinate system is moving with the velocity of SP1 at
2.308 km/s). The flow overexpands from SP1 (about 145
bars) by means of a strong rarefaction wave (RW) and forms
a low-pressure (~10-bar minimum) supersonic wall jet (see
the Mach number contours, relative to SP1, of Fig. 4c).

The gas velocity in the wall jet (3.5 to 4.3 km/s) is
larger than the wave velocity of the Mach stem (~2.75
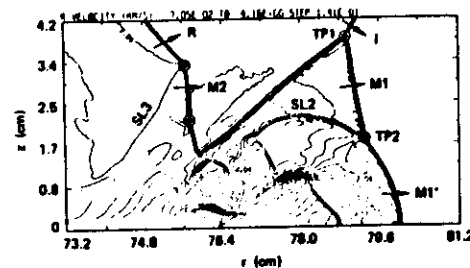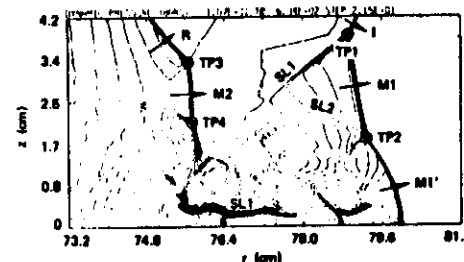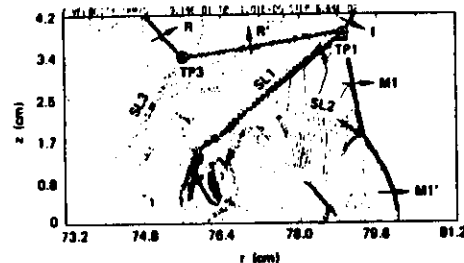km/s), so the jet rams into the rear of the Mach stem.

Fig. 4a   Shock structure
in the double-Mach reflec-
tion regime (t = 270 μs,
Mach stem at 80 cm).

Fig. 4b   Shock structure
in the double-Mach reflec-
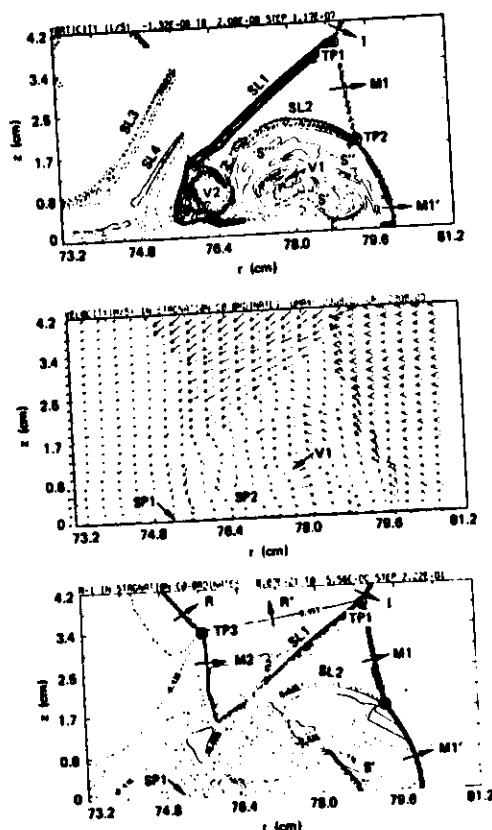tion regime (t = 270 μs,
Mach stem at 80 cm).

Fig. 4c   Shock structure
in the double-Mach reflec-
tion regime (t = 270 μs,
Mach stem at 80 cm).

This interaction pushes out the foot of the Mach stem and
forces the jet to expand upward two dimensionally, thus
forming a rotational flow and a main vortex V1, which has
positive rotation. The rotational flow near V1 is locally
supersonic, and embedded shocks (S', S'', and S''') can be
seen.

The toeing-out of the Mach stem creates a second
triple point, TP2. This is actually an inverted Mach stem
structure with an incident shock M1', a reflected shock
S'', a Mach stem M1, and a slip line SL2 that has negative
vorticity. This slip line flows up and over the main vor-
tex V1, approaches the wall and stagnates, thus creating a
second moving stagnation point (SP2), which is also evi-
dent in the relative velocity vector plot of Fig. 4c. At
a range of 80 cm, SP2 has shocked-up on the wall. All of
slip line SL2 and some of SL1 are entrained in a second
vortex structure V2, which has negative rotation (see

Fig. 4c). All of the fluid entering the main Mach stem M1
between triple points TP1 and TP2 is entrained in vortex
V2 (see the vorticity contour plot of Fig. 4c).

The gas velocity is supersonic above slip line SL1 and
subsonic below it. Pressure waves from SP1 coalesce,
forming the second Mach stem M2. The latter interacts
with the reflected shock forming a third triple point
(TP3). This also appears to be an inverted Mach structure
with an incident wave R', a reflected wave M2, a Mach stem
R, and a slip line (SL3). A fourth triple point (TP4) can
be seen on shock M2. It appears to be a remnant of the
interaction of the embedded shock S''' with SL1. It has
an incident shock M2, a reflected shock R'', a Mach stem
M2', and a slip line SL4. Shock R'' terminates on slip
line SL3, while shock M2' terminates on slip line SL1.

Secondary vortex structures are evident on slip line
SL1 (caused by shock M2 and local rarefaction waves) and
slip line SL2 (induced by shock S'''), and near vortex V1
(the entrained part of SL1 that was shocked by S'').

The rarefaction wave behind the incident shock propa-
gates through the DMR structure (see, for example, the
density, internal energy, and pressure contour plots of
Fig. 4a) just as in the regular reflection case; but this
appears to be a weak effect, since the main discontinui-
ties (R', SL1, and M2) are basically straight lines.

Even at the 80-cm range, the wall jet was quite thin
(1.8 mm) and not well resolved (about six cells high);
although very fine zoning was used here, it was still too
coarse for adequate numerical resolution. The slip line
SL1 on top of the jet is a free shear layer subject to
Kelvin-Helmholtz instabilities. Here the Reynolds number
of the jet was about $3x10^4$ based on jet height. It will
no doubt develop vortex structures, leading to turbulent
mixing. Also, the wall boundary layer will reduce the
radial momentum of the jet. Hence, turbulence effects
will influence the entrainment of the main vortex V1 and
the toeing-out of M1' (i.e., there will be less pushing).
These effects were not modeled in this calculation and
may, in fact, influence transition.

F. Surface Data

Figure 5 gives a detailed snapshot of the complete
flowfield on the surface at the end of regular reflection
(t = 171 μs, reflection point at 50 cm) and in the fully
resolved double-Mach region (t = 270 μs, Mach stem toe at
80 cm). Such plots augment the interpretation of the con-
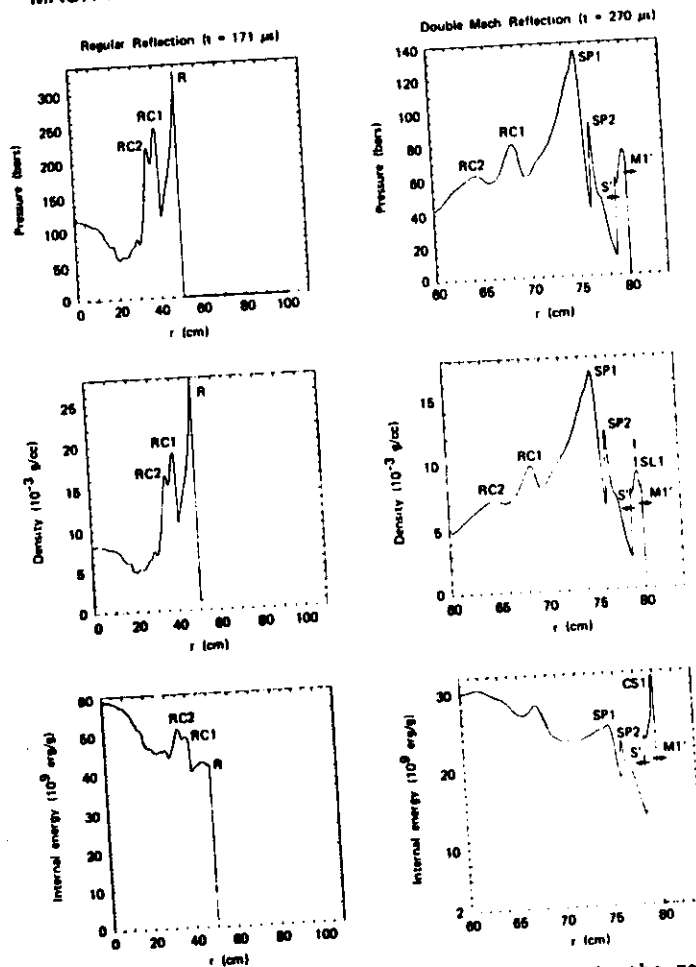tour plots in Figs. 2 and 4. The reflected shocks R, RC1,

Fig. 5a   Comparison of surface-level flowfields in the regular reflection regime (t = 171 μs) and double-Mach reflection regime (t = 270 μs).

Fig. 5b   Comparison of surface-level flowfields in the regular reflection regime (t = 171 μs) and double-Mach reflection regime (t = 270 μs).

and RC2 (as well as additional wave structures near the origin) can be seen. Both RC1 and RC2 reside in the coarse-zoned region at these times; hence they appear somewhat diffused.

In the double-Mach region, the main features of the flow are sharp and well resolved. Moving stagnation points SP1 and SP2, the shocks M1' and S', and the slip surface SL1 are clearly visible. The gas overexpands from stagnation point SP1, reaching a maximum velocity of about 4.2 km/s (Mach number of about 5.4) before it is shocked
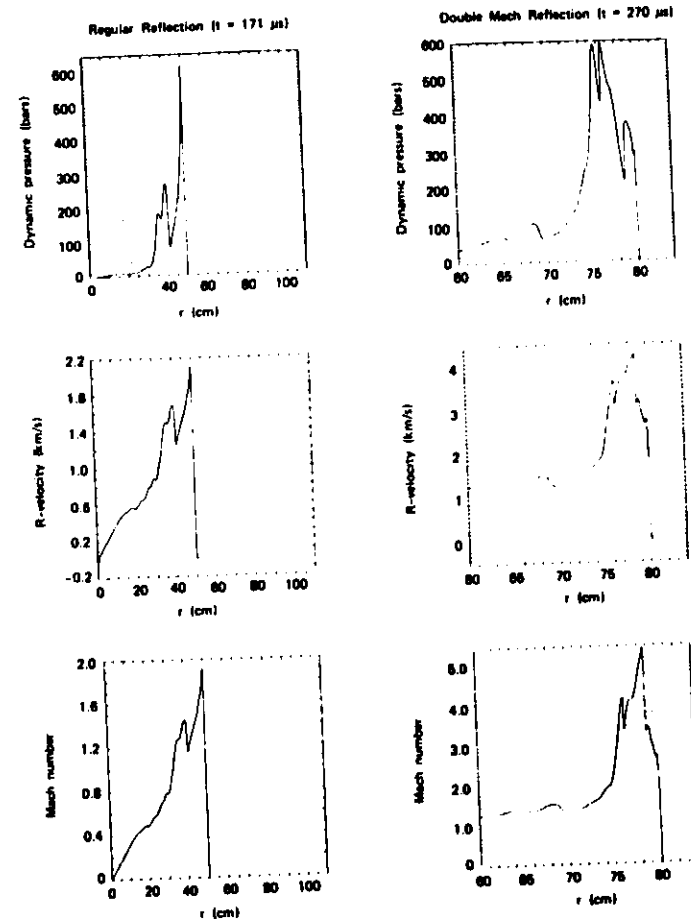
by S', thereby becoming compatible with conditions behind M1'.

In effect, the double-Mach structure focuses the blast energy toward the surface, thereby greatly extending the high enthalpy flow region. For example, dynamic pressures of 600 bars, pitot pressures of 1200 to 1400 bars, and total enthalpy of nearly 10^{11} erg/g seen in the regular reflection region at 50 cm are extended to a ground range of 80 cm as a result of the double-Mach flowfield.

The calculated surface-level peak overpressures of the various shocks are plotted as a function of ground range
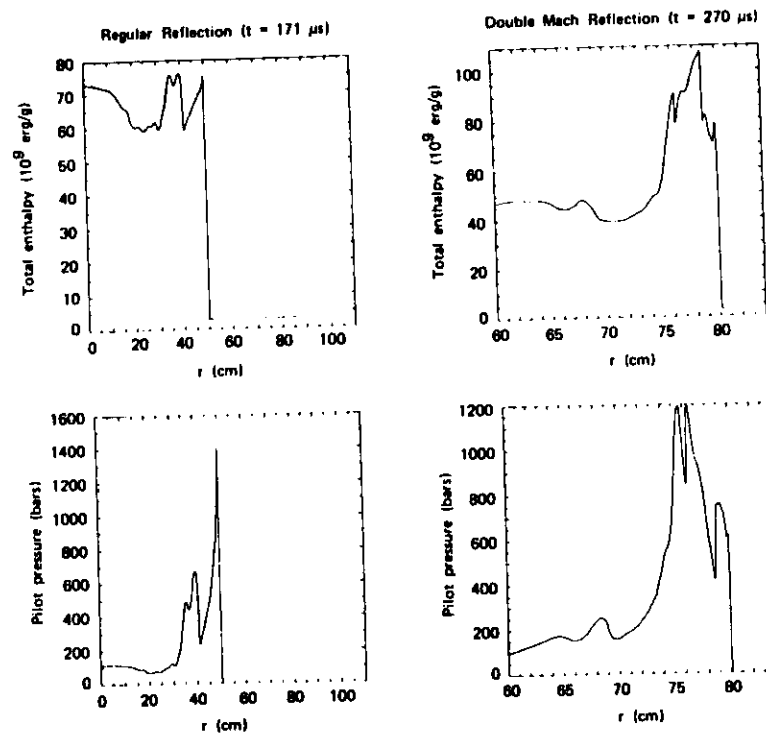
Fig. 5c   Comparison of surface-level flowfields in the regular reflection regime (t = 171 μs) and double-Mach reflection regime (t = 270 μs).

Fig. 6)   Comparisons of calculated peak pressures on the surface with experimental data (Carpenter 1974).

in Fig. 6. The incident overpressure at ground zero of 98.86 bars reflects to a peak value of 880 bars. The corresponding theoretical reflection factor for real air is 9.43, which results in a theoretical reflected pressure of 932 bars (vs 880 bars for the two-dimensional calculation, or 6 percent low due to zoning). The reflected pressure curve R agrees very well with the experimental data of Carpenter (1974), thus indirectly confirming that the calculated incident blast wave closely simulated the experimental blast wave. Near ground zero, the shocks RC1 and RC2 are much stronger than the reflected shock R, but they decay more rapidly. As mentioned before, calculated values for RC1 and RC2 are expected to be too large because of the sharp contact surface in this calculation.

Note in particular that the pressure range curve for shock R suffers a jolt at 49.5 cm (i.e., near the RR limit) and locally increases at 53 cm—this behavior per-
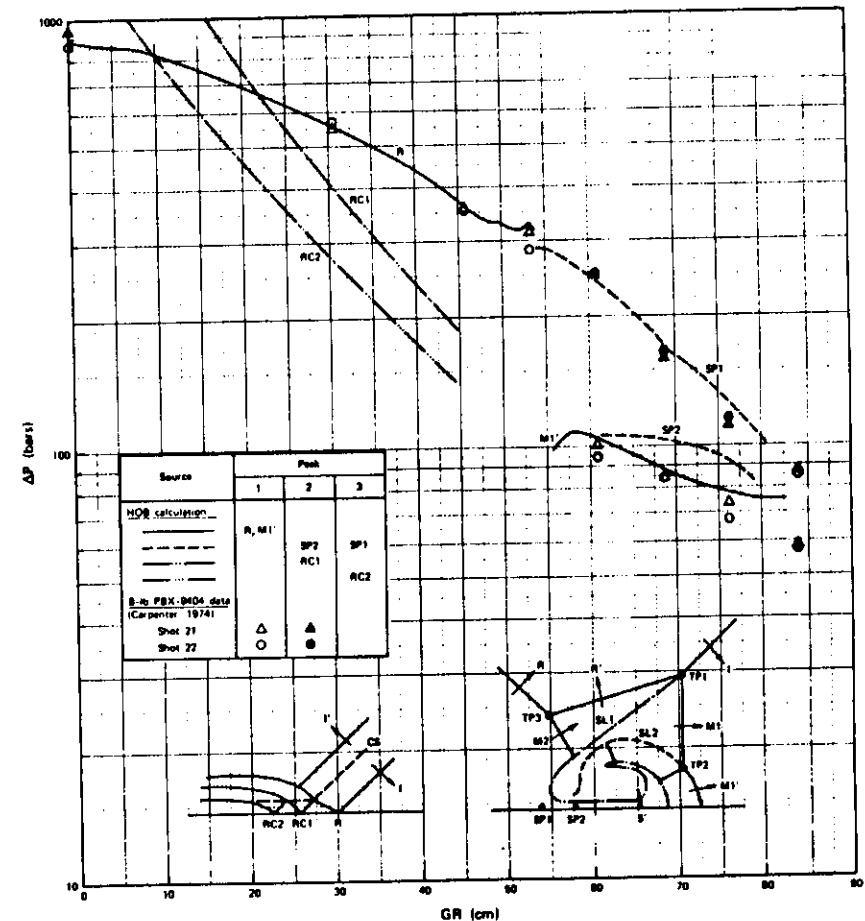
haps being a consequence of the arrival of the sonic point singularity and the formation of a nascent Mach stem.

In the double-Mach region, the main stagnation point SP1 decays from 290 bars at transition to a value of about 100 bars at 80 cm. Stagnation point SP2 and shock M1' decay rather slowly from about 100 bars to 75 bars. In general, the calculated peaks in the double-Mach region are in excellent agreement with the experimental data (Carpenter 1974) even at 53 cm, where the grid points were inadequate to resolving the double-Mach stem.

G. Comparisons with DMR on Wedges

Considerably more is known about the details of double-Mach shock structures created by plane shock reflections from wedges. Such flows have many useful features:

1) The flows are self-similar (two-dimensional Cartesian), and hence are more amenable to analysis.

2) Experimental photographic results (e.g., Schlieren, shadowgraph, and interferometric data) are available to verify code calculations.

3) The complicating effects of a rarefaction wave behind the incident shock are absent.

In addition, wedge results (e.g., reflection factors) are often used to approximate the height-of-burst case. Hence, it is useful to explore the equivalence of the DMR flowfield for the wedge case corresponding to the height-of-burst case.

The double-Mach structure at a time of 270 μs (Mach stem at 80 cm) from the present calculation was selected for comparison. At this time the incident shock Mach number (M_I) was 5.46 with an incident shock angle of about 57 deg. The equivalent wedge case was constructed as follows. A 500x100 y-cell two-dimensional Cartesian mesh was chosen with square zones ($\Delta x = \Delta y = 1$ unit). The shock properties corresponding to an $M_I = 5.46$ real air shock were continuously fed into the left side of the grid at a shock angle of 57 deg (wedge angle of 33 deg). The second-order Godunov scheme (with Gilmore's equation of state for real air) was then used to calculate the reflected flowfield.

The results of the wedge case are shown in Fig. 7. By design, the calculations are identical at the main triple point TP1. The overall features of the wedge flowfield are quite similar to the height-of-burst case (Fig. 4), considering that the wedge case was about 2.4 times more coarsely zoned. Peak pressures on the wall (SP1) were 133 bars (instantaneous value at 75.2 cm) for the height-of-burst case and 122 bars for the wedge, yielding "reflection factors" of 3.8 and 3.5, respectively.

The principal differences are the reflected shock angle and the location of triple point TP3. The reflected shock angle of 49 deg for the height-of-burst case is considerably steeper than the 22-deg angle for the wedge case. In the height-of-burst case, the rarefaction wave behind the incident shock allows the reflected shock R to move upward more easily into the incident wave. This causes the second Mach stem (M2) to be more vertical and
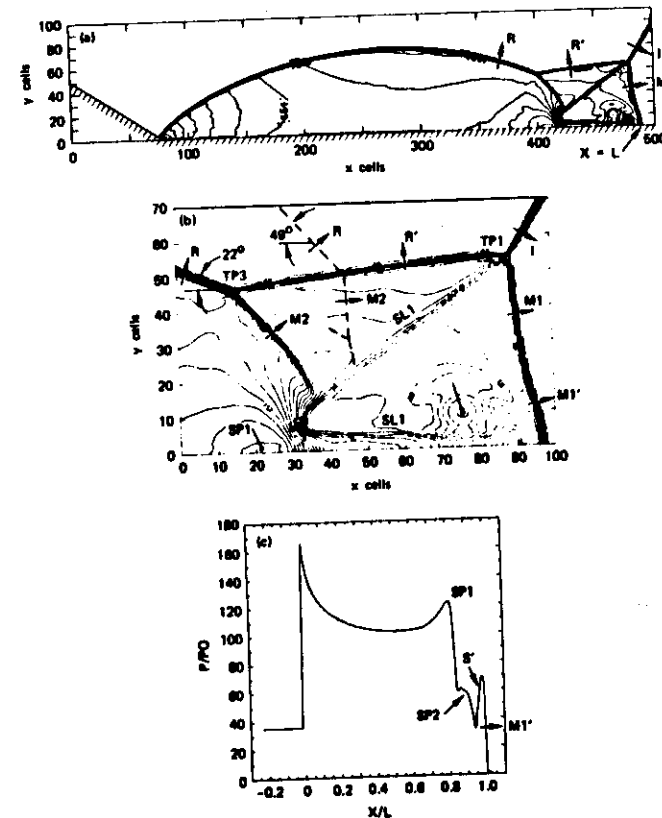
Fig. 7) Double-Mach reflection from a ramp ($M_I = 5.46$, $\theta_W = 33$ deg, Gilmore's air EOS [Gilmore 1955]): (a) Overall density contours; (b) density contours in the double-Mach region (dashed lines correspond to the HOB results at 270 μs); (c) wall pressure distribution.

the length of the reflected shock R' to be about half the value found for the wedge case. (To elucidate these points, shocks M2 and R for the height-of-burst case are depicted as dashed lines on the wedge results.) Consequently, the distance between points SP1 and M1' (i.e., the DMR duration) is somewhat shorter in the height-of-burst case.

In summary, we may conclude that the height-of-burst case is truly nonsteady, and hence not amenable to similarity analysis. The rarefaction wave behind the incident shock modifies the reflected shock angle at TP3 and thereby influences the location and shape of the second Mach stem M2, compared to the equivalent wedge case. Because

peak reflected pressures and "reflection factors" are a consequence of the gasdynamic state at the main triple point, they are similar for the two cases. However, the height-of-burst "reflection factor" $(R=\Delta p_{SP1}/\Delta p_I)$ must be based on instantaneous values (with SP1, TP1, and M1' all being at different radii from the explosion center).

IV. Conclusions

The present calculation demonstrates that the reflection of a spherical HE-driven blast wave from a plane surface creates complex flow structures on multiple length scales. In the regular reflection region, portions of shock R reflect within the channel formed by the wall and the dense detonation products, thus producing additional pressure pulses on the wall. The interaction of shock R with contact surface CS and slip line SL' inviscidly generates vorticity, which leads to the formation of large-scale vortex structures (i.e., turbulent mixing) on the interface between the detonation products and the air. In the double-Mach flow structure, slip lines emanating from the triple points TP1 and TP2 are directed downward. The flow is forced to turn parallel at the wall, thereby converting some of the flow kinetic energy into pressure and creating stagnation points SP1 and SP2 that move with the DMR structure. This also creates a supersonic wall jet consisting of a free shear layer and a wall boundary layer. The Reynolds number of the jet is quite large, ranging from 3×10^4 for this case to 10^7 for large-scale explosions. Hence, one would expect strong turbulent mixing at the free shear layer; however, the wall jet in these calculations was laminar. The second-order Godunov algorithm used here is nondiffusive enough to be able to calculate the evolution of discrete vortex structures started from inviscid Kelvin-Helmholtz instabilities (Glowacki et al. 1986) if adequate zoning is used in the jet (about five times finer than that used here). The wall boundary layer was not modeled. Both effects will influence the horizontal momentum of the jet, the toeing-out of the Mach stem, and the rotational flow of the main vortices V1 and V2. Adaptive gridding and a viscous wall boundary layer capability are needed to accurately model these details.

A double-Mach shock structure appeared in this calculation at a ground range between 52.5 and 55 cm, which was 1.5 to 3.8 deg beyond the limit of regular reflection. We believe that the so-called persistence of regular reflection in this calculation was caused by inadequate computational zoning, whereas the persistence in experiments is

due to viscous wall boundary layer effects. Adaptive gridding and a viscous wall boundary layer capability are again needed to accurately calculate such flows.

The double-Mach shock structure directs some of the blast energy toward the surface, and thereby extends the high enthalpy flow to larger ground ranges. The calculated surface-level peak pressures are in excellent agreement with experimental data at all ground ranges.

A shock-on-wedge calculation was also performed to simulate the double-Mach flowfield from the height-of-burst case at $t = 270$ μs (Mach stem at 80 cm). Overall features of the flow were quite similar in both cases. The principal differences were the reflected shock angle, which was larger in the height-of-burst case; and the location of triple point TP3, which was closer to TP1 in the height-of-burst case. These effects were attributed to the incident wave rarefaction effects and true nonsteadiness of the height-of-burst case.

References

Ando, S. and Glass, I.I. (1981) Domains and boundaries of pseudostationary oblique-shock-wave reflections in carbon dioxide. Proceedings of the 7th International Symposium on the Military Applications of Blast Simulation, pp. 3.6-1 to 3.6-24. Defence Research Establishment, Suffield, Ralston, Alberta, Canada, V.I.

Anisimov, S.I., Zel'dovich, Y.B., Inogamov, N.A., and Ivanov, M.F. (1983) The Taylor instability of contact boundary between detonation products and a surrounding gas. Shock Waves, Explosions and Detonations, edited by J.R. Bowen et al. Progress in Astronautics and Aeronautics, 87, AAIA, New York.

Baker, W.E. (1973) Explosions in Air. University of Texas Press, Austin, Texas, pp. 118-149.

Bazhenova, T.V., Gvozdeva, L.G., and Nettleton, M.A. (1984) Unsteady interactions of shock waves. Prog. Aerosp. Sci. 21, 249-331.

Ben-Dor, G. and Glass, I.I. (1978) Nonstationary oblique-shock-wave reflections: Actual isopycnics and numerical experiments. AIAA J. 16(11), 1146-1153.

Ben-Dor, G. and Glass, I.I. (1979) Domains and boundaries of nonstationary oblique-shock-wave reflexions. 1. Diatomic gas. J. Fluid Mech. 92 (12 June), 459-496.

Berger, M. and Colella, P. (1986) Local adaptive mesh refinement for shock hydrodynamics (in press).

Bertrand, B.F. (1972) Measurement of pressure on Mach reflection of strong shock waves in a shock tube. Mun. Report 2196, Ballistics Research Laboratory, Aberdeen, Md.

Bleackney, W. and Taub, A.H. (1949) Interaction of shock waves. Rev. Mod. Phys. 21(Oct.), 584-605.

Brode, H.L. (1955) Numerical solutions of spherical blast waves. J. Appl. Phys. 26(6), 766-775.

Brode, H.L. (1959) Blast wave from a spherical charge. Phys. Fluids. 2(2), 217-229.

Carpenter, H.J. (1974) private communication. Carpenter Research Corporation, Palos Verdes, Calif.

Colella, P. and Glaz, H.M. (1984) Numerical computation of complex shock reflections in gases. Proceedings of the 9th International Conference on Numerical Methods in Fluid Dynamics, Saclay, France, edited by F. Soubbaramayer and J.P. Boujot. Springer-Verlag, Berlin.

Colella, P. and Glaz, H.M. (1985) Efficient solution algorithms for the Riemann problem for real gases. J. Comput. Phys. 59(2), 264-289.

Colella, P., Glaz, H.M., and Ferguson, R.E. (1986) Eulerian multi-material transport calculations using the second-order Godunov scheme and SLIC (in press).

Colella, P. and Woodward, P.R. (1984) The piecewise parabolic method (PPM) for gas-dynamical simulations. J. Comput. Phys. 54(1), 174-201.

Courant, R. and Friedrichs, K.O. (1948) Supersonic Flow and Shock Waves. Wiley, New York.

Deschambault, R.L. and Glass, I.I. (1983) An update on nonstationary oblique-shock-wave reflections: Actual isopycnics and numerical experiments. J. Fluid Mech. 131(June), 27-57.

Dobratz, B. (1974) Properties of chemical explosives and explosive simulants. UCRL-51319, University of California-Lawrence Livermore Laboratory, Livermore, Calif.

Fry, M., Picone, J.M., Boris, J.P., and Book, D.L. (1981) Transition to double-Mach stem for nuclear explosion at 104-ft height of burst. NRL Memorandum Report 4630, Naval Research Laboratory, Washington, D.C.

Gilmore, R.R. (1955) Equilibrium composition and thermodynamic properties of air to 24000 K. RM-1543, Rand Corporation, Santa Monica, Calif.

Glass, I.I. (1982) private communication. UTIAS, University of Toronto, Toronto, Canada.

Glaz, H.M. (1979) Development of random choice numerical methods for blast wave problems. NSWC/NOL TR 78-211, Naval Surface Weapons Center, White Oak, Md.

Glaz, H.M., Colella, P., Glass, I.I., and Deschambault, R.L. (1985a) A numerical study of oblique shock-wave reflections with experimental comparisons. Proc. R. Soc. London, Ser. A, 398, 117-140.

Glaz, H.M., Colella, P., Glass, I.I. and Deschambault, R.L. (1985b) A detailed numerical, graphical, and experimental study of oblique shock wave reflections. UTIAS Report 285, University of Toronto, Toronto, Canada.

Glaz, H.M., Glass, I.I., Hu, J.C.J., and Walter, P. (1986) Oblique shock wave reflections in SF6: A comparison of calculation and experiment. 10th International Colloquium on the Dynamics of Explosions and Reactive Systems August 4-9, 1985, Berkeley, California (to be published by AIAA).

Glowacki, W.J., Kuhl, A.L., Glaz, H.M., and Ferguson, R.E. (1986) Shock wave interactions with high sound speed layers. Proceedings of the 20th Shock Tube Symposium, 29 July-2 Aug, 1985, Berkeley, California (forthcoming).

Hansen, C.F. (1959) Approximations for the thermodynamic and transport properties of high-temperature air. NASA TR R-50.

Henderson, L.F., and Lozzi, A. (1975) Experiments on transition of Mach reflexion, Part 1. J. Fluid Mech. 68(11 Mar.), 139-155.

Hornung, H. (1985) Regular and Mach reflection of shock waves. Ann. Rev. Fluid Mech. 18, 33-58.

Hornung, H.G. and Taylor, J.R. (1982) Transition from regular to Mach reflection of shock waves. Part 1. The effect of viscosity in the pseudosteady case. J. Fluid Mech. 123(Oct.), 143-153.

Hu, J.T.C. and Glass, I.I. (1986) An interferometric and numerical study of pseudostationary oblique-shock-wave reflections in sulfur hexafluoride (SF6). Proc. R. Soc. London (to be published).

Kuhl, A.L. (1982) private communication. R & D Associates, Marina del Rey, Calif.

Kuhl, A.L. and Seizew, M.R. (1978) Analysis of ideal, strong Chapman/Jouguet detonations. TRW Tech. Rept. 78.4735, 9-1, TRW Systems, Redondo Beach, Calif.

Korobeinikov, V.P. and Chushkin, P.I. (1966) Plane, cylindrical, and spherical blast waves in a gas with counterpressure. Proceedings, Steklov Institute of Mathematics. Akademiya Nauk, Moscow, SSSR, pp. 4-33.